High-Resolution Holographic Microscopy Exploiting Speckle-Correlation Scattering Matrix

YoonSeok Baek,[1,2] KyeoReh Lee,[1,2] and YongKeun Park[1,2,3,*]

[1]*Department of Physics, Korea Advanced Institute of Science and Technology, Daejeon 34141, Republic of Korea*
[2]*KAIST Institute for Health Science and Technology, KAIST, Daejeon 34141, Republic of Korea*
[3]*Tomocube, Daejeon 34051 Republic of Korea*

Using a conventional refraction-based optical lens, it is challenging to achieve both high-resolution imaging and long-working-distance conditions. To increase the numerical aperture of a lens, the working distance should be compensated and vice versa. Here we propose and demonstrate a new concept in optical microscopy that can achieve both high-resolution imaging and long-working-distance conditions by utilizing a scattering layer instead of refractive optics. When light passes through a scattering layer, it creates a unique interference pattern. To retrieve the complex amplitude image from the interference pattern, we utilize a speckle-correlation scattering-matrix method. The proposed method enables holographic microscopy without any lens or external reference beam. Importantly, it allows high-resolution imaging with a long working distance beyond that which a conventional objective lens can achieve. As an experimental verification, we image various microscopic samples and compare their performances with off-axis digital holographic microscopy.

I. INTRODUCTION

In optical microscopy, the performance of an objective lens is greatly affected by the size of an aperture. A finite-lens aperture forces a fixed relationship between a numerical aperture (NA) and a working distance. Thus, when the aperture size is fixed, there is a trade-off between NA improvement and improvement in a working distance, which becomes a critical issue when a high resolution and a long working distance cannot be compromised, such as imaging of a thick tissue, an extracellular matrix [1], or a microfluidic channel [2].

A straightforward solution is to expand the physical size of the aperture [3–5]. In reality, however, this approach is impractical because aberration becomes severe with increase in the aperture size. In addition an objective becomes bulky and heavy causing compatibility issues. For this reason increasing the aperture size is challenging and costly, and alternative approaches have been introduced. For example, Fourier ptychography [6,7] can mitigate the issue by simulating a large-aperture imaging system. It allows high-resolution imaging with a low-NA objective lens that typically has a long working distance. However, it requires a thin sample [8], and a heavy computational workload is unavoidable.

A possible alternative to the existing solution is to exploit multiple scattering of light in a disordered medium.

Multiple scattering is a deterministic process that is described by a scattering matrix or a transmission matrix (TM) in a transmission geometry [9–11]. Recent studies have demonstrated that a scattering layer can be used for focusing and imaging by utilizing the information of a TM [12–17]. A TM is also utilized in laser-scanning microscopy to generate optical foci through a scattering layer [18–21]. Importantly, TM-based imaging has been introduced in microscopy yielding an improved resolution beyond what a refraction-based imaging system with an objective lens can achieve [22,23]. However, TM-based imaging methods require a complicated interferometric system. Alternatively, microscopic imaging using a scattering layer has been demonstrated [24] by exploiting speckle correlations [25,26]. However, its use is limited to the imaging of sample intensity at a fixed axial position.

Here we demonstrate a high-resolution long-working-distance reference-free holographic microscopy using a scattering layer. The scattering layer simultaneously replaces the roles of an objective lens and that of an interferometer (Fig. 1). Exploiting the speckle-correlation scattering matrix (SSM) technique [27], the scattering layer can be utilized as a high-NA imaging lens with a long-working-distance condition. This is possible because the scattering layer only needs to generate random speckles. As a result, a large-size scattering layer can be easily adopted unlike the case of a conventional objective lens. By exploiting the randomness of a multiple-scattering layer, SSM uniquely determines an incident
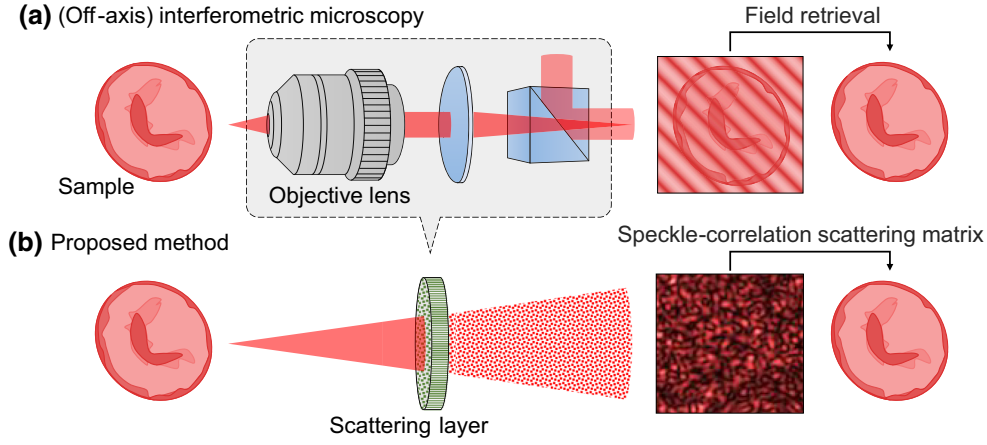
*yk.park@kaist.ac.kr

024053-1

FIG. 1. Comparison between conventional interferometric microscopy and the proposed method. (a) Schematic of off-axis-interferometric microscopy. An objective lens is used to collect diffracted light from a sample with a high-numerical aperture. In addition, an external reference beam should be introduced to perform interferometry. The complex amplitude at the sample plane is retrieved from the measured interferogram. (b) A schematic of the proposed method is shown. In the proposed method, the optical components are replaced with a single scattering layer. The scattering layer generates a unique interference pattern, from which the complex amplitude is retrieved using the speckle-correlation scattering matrix technique.

field from the scattered-intensity image of light after passing through a scattering layer. This allows holographic imaging of a microscopic object without introducing a reference beam for off-axis interferometry. We experimentally demonstrate a high-NA (0.7) with a working distance of 13 mm, which significantly exceeds the capabilities of existing commercially-available high-NA and long-working-distance objective lenses. The performance of the proposed method is demonstrated by imaging various microscopic samples.

II. PRINCIPLE

The principle of the proposed method is based on SSM. SSM is a method to retrieve the complex amplitude of an incident light from an intensity image of light transmitted through a scattering layer. SSM essentially utilizes the TM information of a scattering layer. The TM, denoted as T, describes the relationship between an incident field x and a transmitted field y, as $y = Tx$. In order to determine an incident field, one must know the transmitted field or vice versa. However, SSM provides a method to retrieve the incident field directly from the intensity image of a random-speckle field [27].

Suppose there is an incident field $x = \sum_n^N \alpha_n k_n$, where k is a spatial frequency or generally an arbitrary orthonormal basis. The corresponding field after a scattering layer can be deterministically described using the TM of the scattering layer as $y = Tx = \sum_n^N \alpha_n t_n = \sum_n^N \alpha_n T k_n$. Then matrix Z can be defined as

$$Z_{nm} = \frac{1}{\langle |t_n|^2 \rangle_r \langle |t_m|^2 \rangle_r} (\langle t_n^* t_m y^* y \rangle_r - \langle t_n^* t_m \rangle_r \langle y^* y \rangle_r), \quad (1)$$

where $y^* y$ corresponds to an intensity image of the transmitted field and $\langle \ \rangle_r$ indicates a spatial average. Note that the Z matrix contains the TM and the measured intensity image. For a strong scattering medium whose TM is described as a Gaussian random matrix [11,28], the fourth-order moment of the Z matrix can be rewritten in terms of second-order moments according to the Isserlis' theorem [29–32]. The fourth-order moment in Eq. (1) can be rewritten as

$$Z_{nm} = \alpha_n \alpha_m^* + \frac{\langle t_n^* y^* \rangle_r \langle t_m y \rangle_r}{\langle |t_n|^2 \rangle_r \langle |t_m|^2 \rangle_r}, \quad (2)$$

where $\alpha_n = \langle t_n^* y \rangle_r / \langle |t_n|^2 \rangle_r$. The second term in Eq. (2) is negligible when the columns of the Gaussian random TM are uncorrelated to each other, i.e., $\langle t_n t_m^* \rangle_r \sim \delta_{nm}$ and $\langle t_n t_m \rangle_r \sim 0$ (see Appendix A for a rigorous condition for uncorrelated TM). In practice, however, the second term can be neglected with an additional condition, as the averaging over all space is impractical due to the limited number of pixels in a detector. This additional condition is an oversampling to keep the number of detection modes (the number of speckles imaged by a detector) larger than the number of input modes (or the number of basis states for the incident field) [27]. If the above conditions are met, Eq. (2) is written simply as $Z = \alpha \alpha^*$, whose singular vector corresponds to the incident field (see Appendix B for the effect of the oversampling).

In principle, there is a single non-zero singular value, and a corresponding singular vector is used to reconstruct the incident field. However, in the presence of noise, there is more than one non-zero singular value. In this case, the
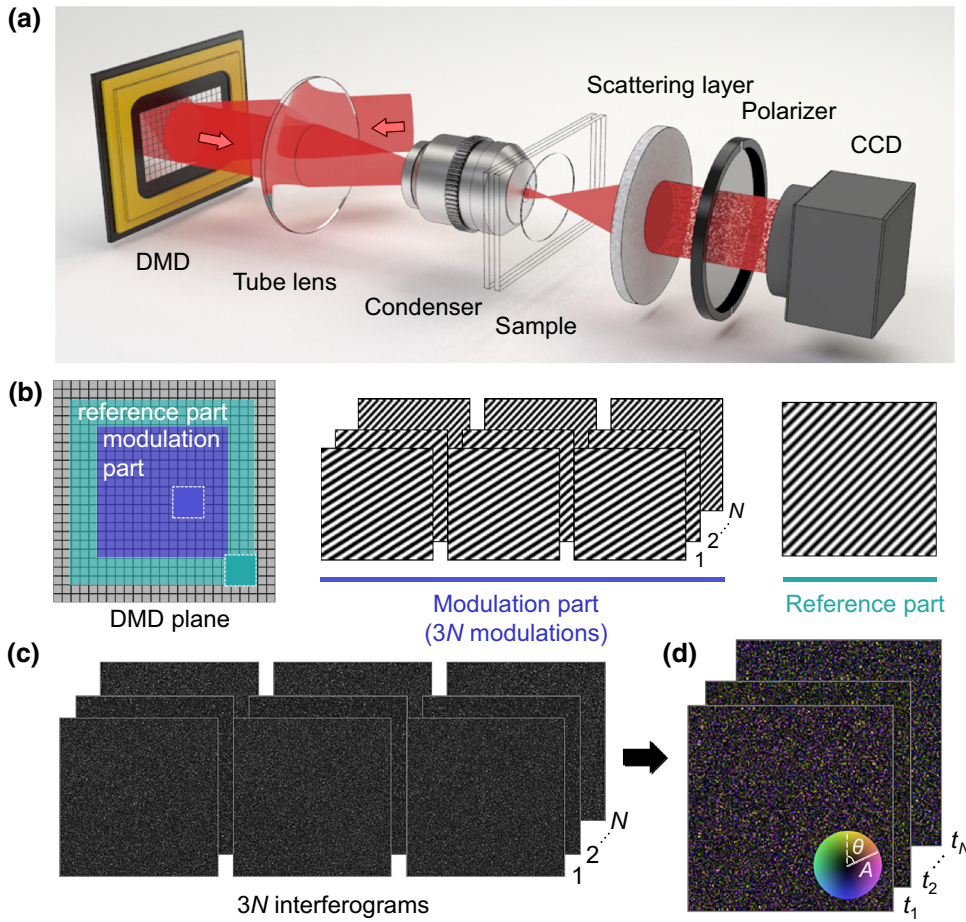
FIG. 2. Experimental setup and TM calibration. (a) Experimental setup with a He-Ne laser (633 nm) used as a light source. The arrows indicate the direction of light propagation. (b) DMD patterns for TM calibration. The central part of the DMD is modulated with $3N$ different patterns, where N is the number of total input modes. In the peripheral part, a static pattern is projected that serves as a reference field. (c) Measured speckle intensity patterns. Three speckle patterns per input mode are measured. (d) TM calculated from the measured speckle-intensity patterns.

singular vector having the largest singular value is used instead.

III. METHODS

A. Experimental setup

The experimental setup is shown in Fig. 2(a). A collimated He-Ne laser (HNL210L, Thorlabs, New Jersey, USA) illuminates a digital micromirror device (DMD) (DLi4130, Digital Light Innovations, Texas, USA). The incident light is diffracted by a grating pattern displayed on the DMD. The diffracted light is captured by a plano-convex lens ($f = 300$ mm). Only the first-order diffraction passes through the condenser lens (UPLFLN60X, Olympus, Tokyo, Japan). Other diffraction orders are filtered out by the back aperture of a condenser. As a result, only the first-order diffraction is imaged in a sample plane. This light illuminates a sample and propagates onto the scattering layer (see Appendix C for the fabrication and optical properties of a scattering layer). The scattered light passes through a linear polarizer to generate a speckle pattern at the CCD (Lt365R, Lumenera, Ontario, Canada).

B. TM calibration

For the calibration of TM, the DMD is divided into two parts [Fig. 2(b)]. One is a modulation part at the center of the DMD. The modulation part corresponds to a field-of-view (FOV) to be calibrated and it projects grating patterns with different spatial frequencies. As only the first-order diffraction passes through the condenser lens, the grating patterns modulate the incident angle of light in the sample plane. The other is a reference part surrounding the central area. The reference part projects a stationary grating pattern throughout the calibration process, providing a static reference field, similar to Refs. [11,17,33]. To maximize the visibility of speckle images, the size of the reference part is determined to have the same surface area as the modulation part.

The total number of patterns used for calibration is determined by the number of input modes (N). For each input mode, three different patterns are used, resulting in phase shifts of 0, $2\pi/3$, and $4\pi/3$. In addition, the intensity image of a reference field is imaged by turning off the modulation part. Thus, a total of $3N+1$ grating patterns are used. The number of input modes depends on the area of a FOV, denoted as A_{FOV}, and the NA to be calibrated. For

example, in the experiment, the number of input modes is expressed as $N \sim \pi\, A_{\text{FOV}}\,(\text{NA}/\lambda)^2$.

From the $3N$ interferograms, we reconstructed the TM by a least-squares matrix inversion [34] as

$$
\begin{pmatrix} |R|^2 + |t_n|^2 \\ R^* t_n \\ R t_n^* \end{pmatrix} = \begin{bmatrix} 1 & e^{i0} & e^{-i0} \\ 1 & e^{i2\pi/3} & e^{-i2\pi/3} \\ 1 & e^{i4\pi/3} & e^{-i4\pi/3} \end{bmatrix}^{-1} \begin{pmatrix} I_{n,0} \\ I_{n,2\pi/3} \\ I_{n,4\pi/3} \end{pmatrix},
$$

$$(3)$$

where R is the reference field, t_n is a nth column of a TM, and $I_{n,\varphi}$ indicates an interferogram with the phase shift of φ corresponding to t_n.

We consider the second element ($R^* t_n$) as a calibrated TM. Note that the columns of the calibrated TM are multiplied with the complex conjugate of the reference field, making it different from the columns of the actual TM (t_n), similar to what was measured in Ref. [11]. However, this does not affect the validity of the method for the following reason. When $R^* t_n$ is used for Eq. (1) instead of t_n, every term inside the bracket, $\langle\ \rangle_r$, is multiplied by a weighting factor, $|R|^2$. Thus by compensating this weighting factor, a correct Z matrix can be obtained. Since the weighting factor is the intensity image of the reference field measured during calibration, the compensation is achieved simply by dividing the weighting factor before taking the spatial average in Eq. (1).

In the experiment, the total number of input modes used in the calibration is 657, which corresponds to a FOV of $15 \times 15\ \mu\text{m}^2$ and an NA of 0.6 for a He-Ne laser (633 nm). The number of detection modes is 502 400. The TM calibration process took 394.2 s using 1971 4-bit patterns.

It should be noted that other TM measurement techniques and configurations can be adopted. For example, one of input modes can be used as a reference instead of a spatially-separated reference [35,36]. These techniques make the most of the degree-of-freedom given by any spatial light modulator, which will be useful when a larger number of input modes is required. Alternatively, the TM can be measured using a Mach-Zehnder interferometer [23,28,37] or a phase-retrieval algorithm [38].

C. Iterative algorithm

In practice the singular vector of Z suffers from speckle noise. This is because the second term of Eq. (2) does not completely vanish. To suppress this noise, we adopt an iterative algorithm. The iteration is processed as follows. The singular vector (α) of the Z matrix having the largest singular value is obtained by singular-value decomposition. Then the obtained singular vector is multiplied by the calibrated TM ($R^* t_n$). This gives a transmitted field ($R^* y$), whose intensity should be identical to the speckle image of a sample multiplied by the intensity image of the reference field ($|R|^2 |y|^2$). Therefore, we replace the amplitude

of the transmitted field with the square root of the multiplied images. Finally, the replaced field is multiplied by the inverse TM. This, in turn, gives an updated singular vector. This process is repeated until no significant update is made to the singular vector. In the experiment, the iteration is set to stop when the correlation between a $(N-1)$th singular vector and a Nth singular vector has a correlation above 0.99999.

IV. RESULTS

A. Experimental demonstration

To demonstrate the performance of the proposed method, we image various samples including a 1951 United States Air Force (USAF) resolution target (no. 59-153, Edmund Optics, New Jersey, USA), a quantitative-phase microscopy target (Benchmark Technologies, Massachusetts, USA), and a human red blood cell (RBC). The experiments are conducted in the following order. First, the TM of a scattering layer is calibrated. When a coverslip is used, TM is calibrated with empty coverslips placed at the sample plane to minimize possible aberration induced by the coverslips.

After the calibration process, samples are placed in the calibrated field of view (FOV). Then the calibrated FOV is illuminated with a plane wave (see Appendix D). The corresponding images of light that passes through the scattering layer are recorded with a CCD. Finally, the complex amplitude at the sample plane is retrieved using SSM.

The experimental results are shown in Fig. 3. The leftmost column in Fig. 3 shows images of the scattered light after passing through the scattering layer for different samples. Each sample generates a completely different speckle pattern. We applied SSM and the iterative algorithm to the speckle images to retrieve the complex amplitudes. For the iterative algorithm, all data converge within 20 steps and require less than a minute of computation time. The results provide visualizations of samples, but speckle noise is present in both the amplitudes and phases [Fig. 3(b)]. The speckle noise arises from the low signal-to-noise ratio (SNR) at weak speckles during the TM calibration. The NA at this point is 0.6, which is determined by TM calibration. For this reason aperture synthesis is adopted to give a coherent summation of the signal. This also leads to an effective NA of 0.7, with an increase of 0.1 (see Appendix E for aperture synthesis). The results following aperture synthesis [39–41] are shown in Fig. 3(c), where speckle noise is greatly suppressed and clear images of the samples are shown.

The first row of Fig. 3 shows results for an amplitude mask from the 1951 USAF resolution target (the third element of the eighth group). The results agree with the standard width of 1.55 μm. The second row corresponds to a quantitative phase-resolution target, which has a height of 200 nm and a refractive index of 1.52. It induces a
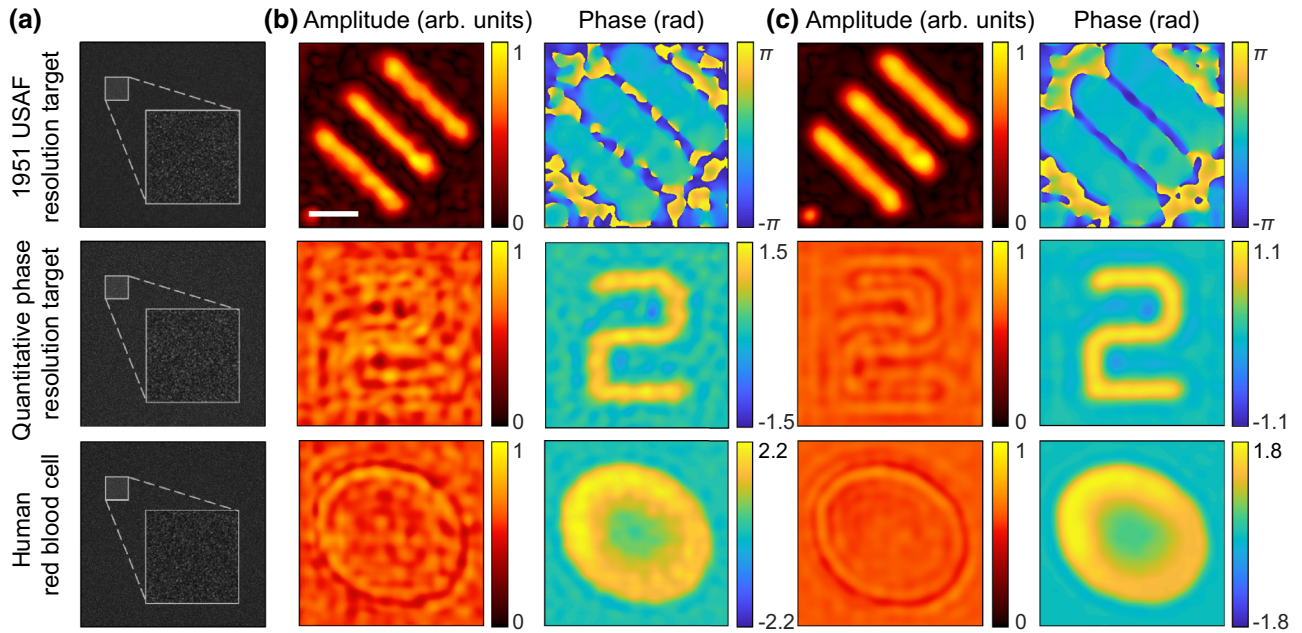
FIG. 3.   Experimental results. (a) Speckle-intensity patterns generated using a scattering layer. (b) Complex amplitude images initially retrieved using SSM and the iterative algorithm applied to (a). (c) Final complex amplitudes retrieved after applying the synthetic aperture method to (b). The first row shows results from a 1951 USAF resolution target (the third element in the eighth group). The second row shows result from the quantitative-phase-resolution target. The third row corresponds to a human red blood cell. The scale bar is 3 μm.

phase delay of 1.03 rad at 633 nm, which agrees with the measured phase value. The third row shows results from a human RBC. The RBC is diluted with Dulbecco's Phosphate-Buffered Saline (DPBS) and sandwiched with a cover slide. The measured phase image agrees well with the known shape of a RBC.

B. High-resolution imaging at a long working distance

The proposed method enables high-resolution imaging at a long working distance, as shown in Fig. 4(a). Since light hitting any position of the surface of the scattering layer undergoes multiple scattering, high-spatial-frequency information can be measured, even at a long working distance. As a demonstration, we image a 5-μm-diameter silica bead (44054, Sigma-Aldrich, Missouri, USA) with the presented method. Then we image the same sample with an off-axis-interferometric microscopy [42,43] adopting a long-working-distance objective (LUC-PLFLN 60X, Olympus, Tokyo, Japan) (see Fig. 5 for the experimental setup of the off-axis-interferometric microscope). The silica beads are immersed in water and sandwiched between two coverslips.

The results from the proposed method and those from off-axis-interferometric microscopy are shown in Figs. 4(b) and 4(c), respectively. The proposed method shows a clear image of a sample. On the contrary, off-axis-interferometric microscopy suffers from aberration of an imaging part induced by an objective lens and

a coverslip. Such aberration artifacts are minimized in the proposed method. This is because any change in wave-front occurring after the sample plane is included in the TM. This can be confirmed by the fact that an aberration-free image of the silica bead shows a good agreement with the results of the proposed method and does not exhibit any aberration artifact that can be found with the long-working-distance objective (see Appendix F).

In addition, the proposed method not only shows a high NA of 0.7, but a significantly improved working distance of 13 mm. This is in contrast with the digital-holographic microscope adopting the long-working-distance objective lens whose NA is 0.7 and whose working distance is 2 mm. Importantly, the proposed method can provide a higher NA and a longer working distance by simply using a larger scattering layer. It should be emphasized that making a large scattering layer does not require careful analysis of aberration unlike the case of an objective lens. The proposed method can be readily adopted as long as a large scattering layer generates uncorrelated speckle patterns.

V. DISCUSSION

In summary, we demonstrate a microscopic technique that simultaneously enables imaging with a high resolution and a long working distance. Exploiting the SSM approach, high-resolution microscopic images of samples are obtained from measurements of speckle intensity
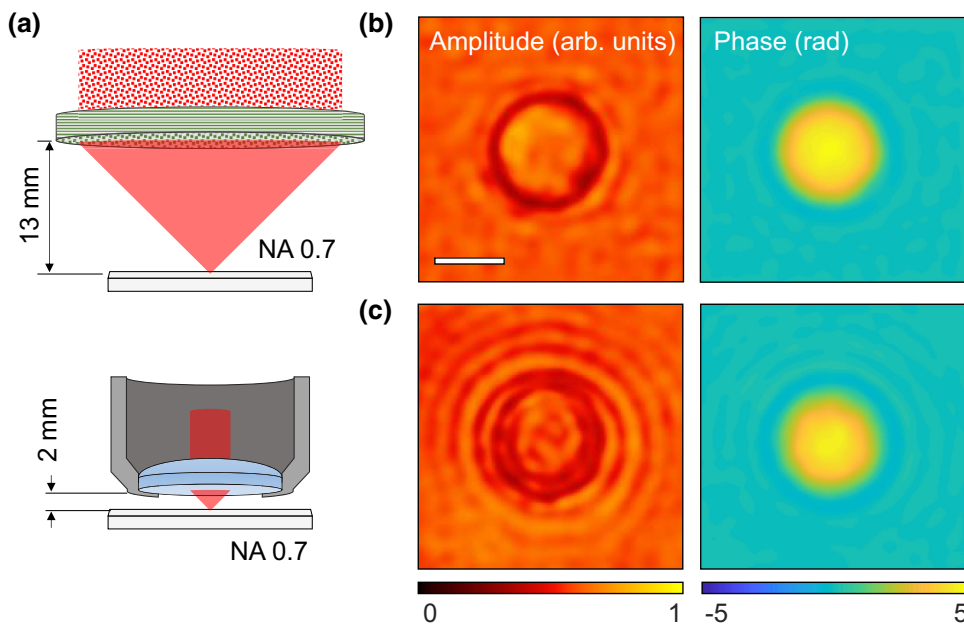
FIG. 4. Comparison of the proposed method and off-axis-interferometric microscopy. (a) The imaging conditions of the proposed method (above) and those in off-axis-interferometric microscopy using a long-working-distance objective lens (below). In this experiment, the proposed method has an NA of 0.7 with a 13-mm working distance. The long-working-distance objective lens has an identical NA (0.7) and 2-mm working distance. (b) The measured complex amplitude for a 5-μm-diameter silica bead using the proposed method. (c) Results from the same sample imaged using off-axis-holographic microscopy with the long-working-distance objective lens. The scale bar is 3 μm.

patterns, which are obtained in a simple optical setup composed of a scattering layer and an image sensor. The scattering layer serves both as an objective lens and an interferometer, and no other optical elements are required for measuring holographic images. With the proposed method, complex amplitudes from various samples are successfully measured from intensity images of light transmitted through the scattering layer. Experimental verification has been conducted with a USAF resolution target, a phase target, and a RBC.

This method provides a unique advantage in quantitative phase imaging and extends the applicability of a scattering layer as an optical element. For example, the proposed method provides highly flexible imaging conditions. The FOV, the NA, or the working distance can be modified through simple calibration. In addition, the calibration can be performed as needed with the same setup used for imaging. Therefore, both calibration and imaging are accomplished without an external reference arm. Consequently, the proposed method enables imaging under different conditions without changing the experimental setup.

The proposed method fundamentally differs from the holographic imaging methods using a scattering layer as reported thus far. Previous methods focused on the use of a memory effect [44–46], the direct use of a TM. The methods based on the memory effect require either a pseudo-thermal light source or an angular scanning of an illumination beam [26,47]. Then an object is retrieved using a phase-retrieval algorithm or a calibrated point-spread function [24,48]. Similarly, a correlation with a known object can be utilized [49]. Nevertheless, they can only retrieve 2D intensity images, not optical fields. Other methods based on TM [22,23,50] require interferometers with external reference beams, which makes an optical system significantly more complicated and limits practical applications. Although adopting a mean-square-optimized operator [17] eliminates the need for an external reference beam, a clear image can be obtained after averaging over many disorder realizations. There has been research to achieve holographic imaging through a scattering layer
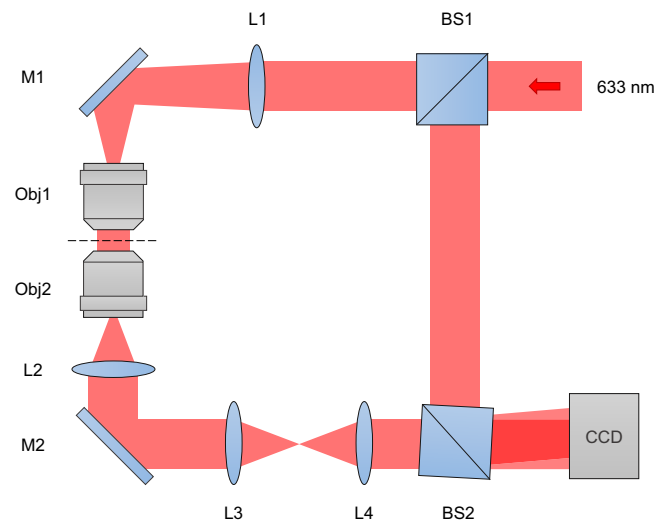

FIG. 5. The experimental setup for off-axis digital-holographic microscopy. L1-L4, lenses; M1-M2, mirrors; Obj1, objective lens (LMPLFLN 50X, Olympus Inc., Tokyo, Japan); Obj2, objective lens (LUCPLFLN 60X, Olympus Inc., Tokyo, Japan); BS1-BS2, beam splitters; CCD (MQ042MG-CM, Ximea, Münster, Germany). Focal lengths of the lenses (L1-L4) are 200, 180, 60, 150 mm, respectively. A 633-nm He-Ne laser (HRR050, Thorlabs, New Jersey, USA) is used as a light source.
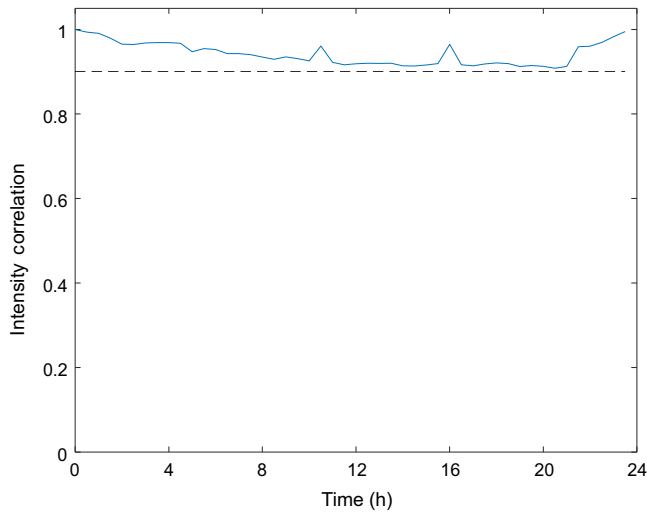
FIG. 6. The stability of the proposed method in the laboratory condition. Temporal intensity correlation between speckle images is measured. The sample plane is illuminated with a plane wave and corresponding speckle images are captured every 30 min. Intensity correlation values are measured with respect to the first speckle image. The correlations are above 0.9 (black dashed line) for 24 h.

using phase conjugation [51–54], statistical averaging [55, 56], or intensity correlations [57–59]. However, in these methods an interferogram must be made with an external reference. Thus a bulky interferometer or a reference beam at the sample plane must be introduced. On the contrary, the proposed method only requires a scattering layer for imaging. The optical field of a sample is incident to the scattering layer without using an external reference beam. The complex amplitude image of a sample is retrieved from an intensity image of the light passed through a scattering layer. Thus, the proposed method allows greater flexibility in the experimental setup.

One limitation of the presented method is that it requires calibration of a scattering layer. However, due to the deterministic nature of multiple-light scattering in complex media, the calibrated scattering layer has a long lifetime provided no changes occur in the scattering medium. Once calibrated, a scattering layer can be used as a high-NA long-working-distance lens. In laboratory conditions, the calibrated information for a scattering later has been used for 24 h without additional calibration (Fig. 6). For high-throughput generation of scattering layers, the photopolymerization of a calibrated scattering layer [60] or an engineered scattering layer [18] can be utilized. In such a case, aberration analysis of an optical setup is required for the correct implementation of the method.

It should be emphasized that the capability of the method is not restricted by the oversampling condition imposed on the number of input and detection modes. This condition appears to limit the amount of measurable information as the number of detection modes cannot be increased indefinitely. However, one can work under this condition using various methods. For example, the NA of the proposed method can be extended beyond the calibrated NA using a synthetic aperture with a large illumination NA [50]. The FOV can also be extended with multiple TMs, each of which corresponds to a different FOV. The feasibility and performance of the method can be further improved with a specially-designed scattering layer whose TM is calibrated in advance [18]. The optimal design can lead to little or no need for postprocessing, including the iterative algorithm and synthetic aperture, by minimizing the correlation between the TM columns.

Finally, the proposed method can potentially be extended to wide applications of digital holographic microscopy (or quantitative phase imaging) [61,62] including holographic particle tracking [63], pathology of cells and tissues [64,65], and quantitative mass imaging [66]. The proposed method can be adopted in the above-mentioned applications without a complex interferometer, but with a flexible imaging condition. We believe that the proposed method can expand the reach of digital holographic microscopy beyond the imaging conditions restricted by an objective lens.

APPENDIX A: RIGOROUS CONDITION FOR UNCORRELATED TM

The retrieval process requires that a TM follow complex Gaussian distribution so that each column is uncorrelated to any other column. The condition of an uncorrelated TM is explicitly studied in [67]. According to the literature, the key parameter that determines the correlation is the conductance, g, and the number of accessible output modes, M. When $g \gg M$ is satisfied, a TM is considered to be uncorrelated.

The conductance, g, can be calculated from the beam size, A_{beam}, incident to the scattering layer and the transmittance of the scattering layer, $\bar{T}$, which is expressed as [67]

$$g \approx 2\pi A_{\text{beam}} \lambda^{-2} \bar{T}. \tag{A1}$$

In the experiment, the beam size in front of the scattering layer has a diameter of 26.5 mm, assuming input modes of TM to be optical foci whose NAs are 0.7. The total transmission through the scattering layer is 2.5%

(See Appendix C). Then the conductance is given by

$$g \approx 2\pi \frac{\pi}{4}(26.5 \text{ mm})^2(633 \text{ nm})^{-2}(0.025)$$

$$\approx 2 \times 10^8. \tag{A2}$$

In the experiment the number of accessible output modes is $M \approx 5 \times 10^5$. Since $g \gg M$, we can safely assume that the TM is uncorrelated.

It should be emphasized that the proposed method works even when columns of the TM are correlated. As long as the TM is a full-rank matrix, we can rewrite the TM with an orthogonal basis for the column space. Then by using the orthogonal basis in Eqs. (1) and (2) of the manuscript instead of the original columns of the TM, the complex amplitude of light can be measured. Thus, the proposed method is not fundamentally limited even when there exists correlation between columns of TM. Nevertheless the condition for an uncorrelated TM is effective because the orthogonal basis can become susceptible to noise when there exists a strong correlation.

In this regard, it is recommended to satisfy two conditions for the proposed method; (1) $g \gg M$, (2) $M > N$, where N is the accessible number of input modes. Combining the two conditions, we get $g \gg N$. Expressions for g and N in terms of system variables are

$$g \approx \frac{2\pi^2}{\lambda^2}\{(\text{WD}) \times \tan(\arcsin(\text{NA}))\}^2 \bar{T}$$

$$\approx \frac{2\pi^2}{\lambda^2}\{(\text{WD}) \times (\text{NA})\}^2 \times (1 - \text{NA}^2)^{-1}\bar{T} \tag{A3}$$

and

$$N = \frac{\pi}{\lambda^2}A_{\text{FOV}}(\text{NA})^2 \tag{A4}$$

where WD is the working distance and A_{FOV} is the area of the FOV at the sample plane. Then $g \gg N$ can be

rewritten as

$$\frac{2\pi(\text{WD})^2}{A_{\text{FOV}}(1 - \text{NA}^2)}\bar{T} > 1. \tag{A5}$$

In conclusion, we can say that the validity of the method is guaranteed by adjusting the imaging conditions.

APPENDIX B: EFFECT OF OVERSAMPLING ON THE RECONSTRUCTION

The second term of Eq. (2) in the main text can be neglected under the condition that the number of detection modes is larger than the number of input modes. For convenience we call the ratio of the number of detection modes to the number of input modes an oversampling ratio in the following discussion. Here we demonstrate how the oversampling affects the reconstruction of the proposed method. We used the same data that are used in Fig. 3 of the main text. The oversampling ratio is modified by changing the size of the image of the transmitted light. Following the retrieval procedure including SSM, the iterative algorithm, and the synthetic aperture method we compare the results at different oversampling ratios.

First, we test with an amplitude object (no. 59-153, Edmund Optics, New Jersey, USA). We change the oversampling ratio to 12, 48, 191, and 765. The results are shown in Fig. 7. At the oversampling ratio of 12, speckle noise is observed. However, at the oversampling ratio of 48, the result provides a clearer image of the sample. As the ratio increases, the speckle noise is further reduced. A similar pattern is found with a phase object (Benchmark Technologies, Massachusetts, USA). Again as the oversampling ratio increases, a clearer image is obtained (Fig. 8). In the experiment, an oversampling ratio of at least 48 guarantees clear imaging of the samples. We expect the minimum-required oversampling ratio can be reduced by improving the SNR of the system or by adopting a transmission matrix that has a minimal correlation between its columns.
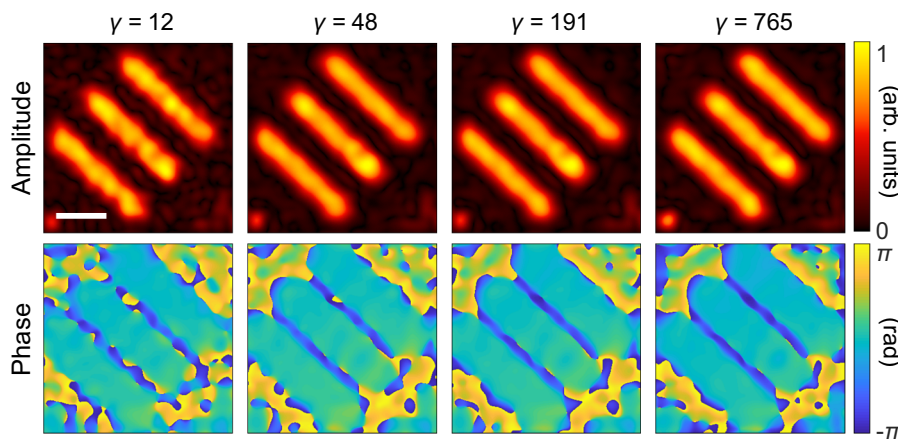

FIG. 7. The effect of oversampling ratio (γ) on an amplitude sample. Amplitudes (upper row) and phases (lower row) at the sample plane with different oversampling ratios are shown. The scale bar indicates 3 μm.

FIG. 8. The effect of oversampling ratio (γ) on a phase sample. Amplitudes (upper row) and phases (lower row) at the sample plane with different oversampling ratios are shown. The scale bar indicates 3 μm.
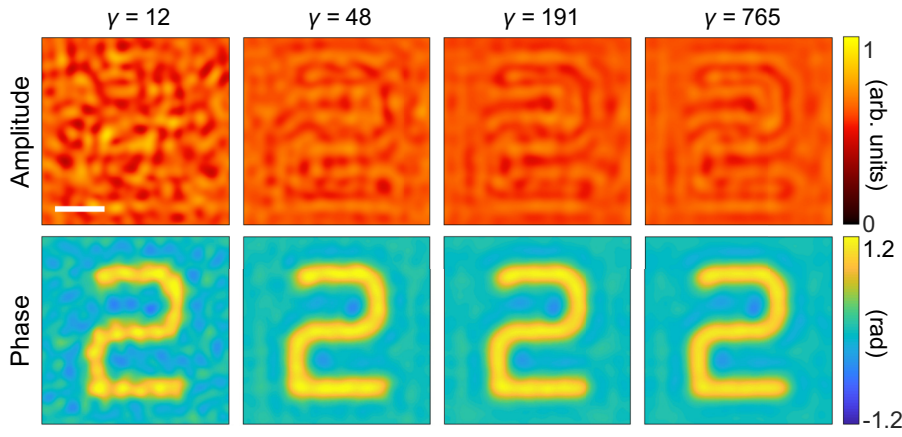
APPENDIX C: FABRICATION AND OPTICAL PROPERTIES OF A SCATTERING LAYER

A rutile (TiO$_2$) paint is made by mixing rutile nanoparticles (637262, Sigma-Aldrich, Missouri, USA), resin (RSN0806, DOW CORNING, Michigan, USA) and solvent (toluene 99%) in a ratio of 0.5 g:1 ml:10 ml. The paint is sonicated for 10 min to disperse the rutile nanoparticles. Then the paint is applied on both sides of a 25-mm-diameter round coverslip by using an air brush (DH-125, Sparmax, Taipei, Taiwan). Finally, the painted coverslip is baked (100 °C, 10 min) to cure the resin. The rutile layer has a thickness of 60 μm and its transmittance is 52%. Its reduced scattering coefficient, μ_s', is 224.9 mm^{-1}, which is measured by inverse adding-doubling [68]. The corresponding mean-free path is 44.5 μm.

To ensure uniform speckle intensity at the CCD, a ground-glass diffuser (DG10-120, Thorlabs, New Jersey, USA) and a circular aperture are used in addition to the rutile-painted layer. The layout of the detection part is shown in Fig. 9. The total transmittance of all components combined is 2.5%.

APPENDIX D: DIGITAL TIME MULTIPLEXING FOR SAMPLE IMAGING

To measure an incident field, the proposed method requires an image of light transmitted through a scattering layer. The image of the transmitted light can be expressed as $I = |TSE_{ill}|^2$, where T is a transmission matrix of a scattering objective, S is a complex amplitude of a sample, and E_{ill} is an illumination field. Here, the illumination field is controlled by a pattern projected on a digital micromirror device (DMD).

Now suppose one wants to measure a sample response with a certain illumination field, E_{ill}. Using the Lee method [69], an approximation of E_{ill} can be achieved. However, the Lee method suffers from noise induced by a binary-amplitude modulation. As a result, the illumination field contains multiple peaks at the Fourier plane, which deteriorates the quality of the reconstructed image.

For this reason we used a digital time-multiplexing method. The digital time-multiplexing method acquires the response of a multi-bit amplitude modulation by digitally synthesizing the response of different binary modulations. The method starts with an N-bit grating-pattern, G (or hologram), which generates E_{ill}. Ideally, G is expressed as $G = e^{ik_c x}E_{ill} + e^{-ik_c x}E_{ill}^*$ with a carrier frequency k_c. First, we divide the grating pattern, G, into series of 1-bit gratings, G_n, which satisfy $G = \sum_{n=1}^{N} 2^n G_n$. Here each 1-bit grating, G, will generate a field $E_{ill}^{(n)}$ satisfying $E_{ill} = \sum_{n=1}^{N} 2^n E_{ill}^{(n)}$. Second, we upload each 1-bit G_n on a DMD and measure corresponding images of the transmitted light, $|TSE_{ill}^{(n)}|^2$. From these images we retrieve $SE_{ill}^{(n)}$ using the proposed method. Finally, we restore the response of E_{ill} by combining the retrieved fields with correct weightings; $SE_{ill} = \sum_{n=1}^{N} 2^n SE_{ill}^{(n)}$. In this way one can measure the response as if the DMD is a multi-bit-depth amplitude modulator.
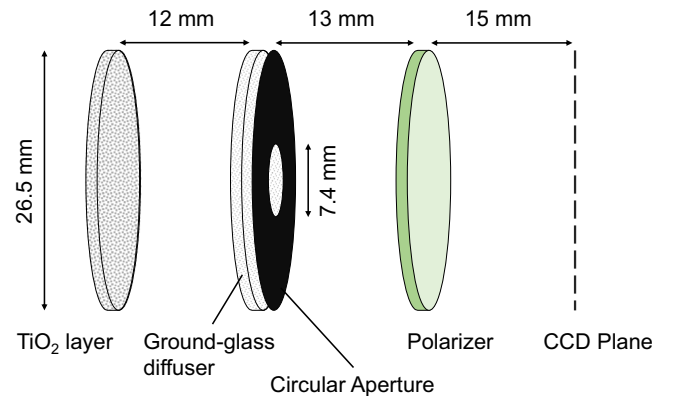

FIG. 9. Layout of detection part. A rutile (TiO$_2$) layer and a ground-glass diffuser is placed at the front spaced 12 mm from each other. A circular aperture is placed right after the ground-glass diffuser to match the speckle size with a size of the CCD pixel. A linear polarizer is placed to ensure linear polarization of scattered light. All components have a diameter of 26.5 mm.

APPENDIX E: SYNTHETIC APERTURE FOR NOISE REDUCTION

First, the complex amplitudes at the sample plane under different illumination angles are measured using SSM and the iterative algorithm. Then we add the measured complex amplitudes together to gain a coherent summation of the signal and an incoherent summation of noise. Since the measured complex amplitudes are shifted differently in Fourier space, such shifts are compensated before the signals are added. For small changes in the illumination angle, the contribution of noise decreases as the number of illuminations (N) increases, i.e., $\sigma_{noise} \propto 1/\sqrt{N}$. In the experiment, 21 different illuminations are used with a maximum illumination NA of 0.1. This gives an increase in the NA by 0.1, resulting in an effective NA of 0.7.

APPENDIX F: COMPARISON WITH AN ABERRATION-FREE IMAGE

To elaborate the result shown in Fig. 4, we imaged a 5-μm-silica bead with the same digital holographic microscope setup used for Fig. 4(c), but a different imaging objective lens (UPLSAPO 60XW, Olympus, Tokyo, Japan). The silica bead is immersed in water and sandwiched between two coverslips for imaging. This objective

lens is not designed for long-working-distance applications. It has a very short working distance of 0.28 mm and the corresponding aperture is smaller than the long-working-distance objective. The experimental result is shown in Fig. 10.

Figures 10(a) and 10(b) show a measured complex image of the silica bead with a native resolution of the objective (NA = 1.2). To simulate the image with an NA of 0.7, the images are low-pass filtered with a cut-off spatial frequency corresponding to an NA of 0.7. The low-pass filtered images are shown in Figs. 10(c) and 10(d). The result shows a clear amplitude and phase image of a sample without the aberration artifact shown in Fig. 4(c). Despite the fact that both objective lenses have correction collars, the comparison shows that a large-aperture objective lens is very vulnerable to the aberration. On the contrary, the low-pass filtered image shows a good agreement with the result shown in Fig. 4(b), indicating that the aberration of the imaging part is minimized with the proposed method.
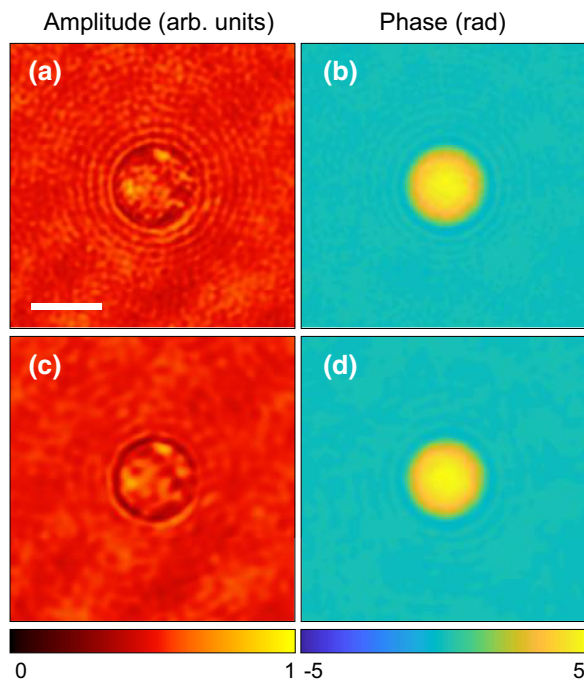

FIG. 10. Complex amplitude images of a 5-μm-silica bead measured with the setup used for Fig. 4 but using a different objective lens (UPLSAPO 60XW, Olympus, Tokyo, Japan). (a),(b) A complex amplitude image of the bead with a native resolution of the objective lens (NA = 1.2) (c),(d) A complex amplitude image obtained by low-pass filtering (a),(b) with a cutoff frequency corresponding to an NA of 0.7. Scale bar 5 μm.

[1] A. Zoumi, A. Yeh, and B. J. Tromberg, Imaging cells and extracellular matrix in vivo by using second-harmonic generation and two-photon excited fluorescence, Proc. Natl. Acad. Sci. U.S.A. **99**, 11014 (2002).

[2] K. E. Herold and A. Rasooly, *Lab on a Chip Technology: Fabrication and Microfluidics* (Caister Academic Press, Norfolk, UK, 2009), Vol. 1.

[3] J. Tan, C. Wang, Y. Wang, W. Wang, J. Liu, R. Leach, and L. Hao, Long working distance microscope with a low obscuration aspherical Schwarzschild objective, Opt. Lett. **39**, 6699 (2014).

[4] S. Pacheco, C. Wang, M. K. Chawla, M. Nguyen, B. K. Baggett, U. Utzinger, C. A. Barnes, and R. Liang, High resolution, high speed, long working distance, large field of view confocal fluorescence microscope, Sci. Rep. **7**, 13349 (2017).

[5] G. McConnell, J. Tragardh, R. Amor, J. Dempster, E. Reid, and W. B. Amos, A novel optical microscope for imaging large embryos and tissue volumes with sub-cellular resolution throughout, eLife **5**, e18659 (2016).

[6] G. Zheng, R. Horstmeyer, and C. Yang, Wide-field, high-resolution Fourier ptychographic microscopy, Nat. Photonics **7**, 739 (2013).

[7] L. Tian, X. Li, K. Ramchandran, and L. Waller, Multiplexed coded illumination for Fourier Ptychography with an LED array microscope, Biomed. Opt. Express **5**, 2376 (2014).

[8] X. Ou, R. Horstmeyer, G. Zheng, and C. Yang, High numerical aperture Fourier ptychography: Principle, implementation and characterization, Opt. Express **23**, 3472 (2015).

[9] A. P. Mosk, A. Lagendijk, G. Lerosey, and M. Fink, Controlling waves in space and time for imaging and focusing in complex media, Nat. Photonics **6**, 283 (2012).

[10] H. Yu, J. Park, K. Lee, J. Yoon, K. Kim, S. Lee, and Y. Park, Recent advances in wavefront shaping techniques

for biomedical applications, Curr. Appl. Phys. **15,** 632 (2015).

[11] S. M. Popoff, G. Lerosey, R. Carminati, M. Fink, A. C. Boccara, and S. Gigan, Measuring the Transmission Matrix in Optics: An Approach to the Study and Control of Light Propagation in Disordered Media, Phys. Rev. Lett. **104,** 100601 (2010).

[12] I. M. Vellekoop, A. Lagendijk, and A. P. Mosk, Exploiting disorder for perfect focusing, Nat. Photonics **4,** 320 (2010).

[13] I. M. Vellekoop and A. P. Mosk, Focusing coherent light through opaque strongly scattering media, Opt. Lett. **32,** 2309 (2007).

[14] J. H. Park, C. Park, H. Yu, J. Park, S. Han, J. Shin, S. H. Ko, K. T. Nam, Y. H. Cho, Y. Park, Subwavelength light focusing using random nanoparticles, Nat. Photonics **7,** 454 (2013).

[15] T. Cizmar and K. Dholakia, Exploiting multimode waveguides for pure fibre-based imaging, Nat. Commun. **3,** 1027 (2012).

[16] H. Yu, K. Lee, J. Park, and Y. Park, Ultrahigh-definition dynamic 3D holographic display by active control of volume speckle fields, Nat. Photonics **11,** 186 (2017).

[17] S. Popoff, G. Lerosey, M. Fink, A. C. Boccara, and S. Gigan, Image transmission through an opaque material, Nat. Commun. **1,** 81 (2010).

[18] M. Jang, Y. Horie, A. Shibukawa, J. Brake, Y. Liu, S. M. Kamali, A. Arbabi, H. Ruan, A. Faraon, C. Yang, Wavefront shaping with disorder-engineered metasurfaces, Nat. Photonics **12,** 84 (2018).

[19] E. G. van Putten, D. Akbulut, J. Bertolotti, W. L. Vos, A. Lagendijk, and A. P. Mosk, Scattering Lens Resolves Sub-100 nm Structures with Visible Light, Phys. Rev. Lett. **106,** 193905 (2011).

[20] G. Ghielmetti and C. M. Aegerter, Scattered light fluorescence microscopy in three dimensions, Opt. Express **20,** 3744 (2012).

[21] G. Ghielmetti and C. M. Aegerter, Direct imaging of fluorescent structures behind turbid layers, Opt. Express **22,** 1981 (2014).

[22] C. Park *et al.*, Full-Field Subwavelength Imaging Using a Scattering Superlens, Phys. Rev. Lett. **113,** 113901 (2014).

[23] Y. Choi, T. D. Yang, C. Fang-Yen, P. Kang, K. J. Lee, R. R. Dasari, M. S. Feld, and W. Choi, Overcoming the Diffraction Limit Using Multiple Light Scattering in a Highly Disordered Medium, Phys. Rev. Lett. **107,** 023902 (2011).

[24] A. K. Singh, G. Pedrini, M. Takeda, and W. Osten, Scatterplate microscope for lensless microscopy with diffraction limited resolution, Sci. Rep. **7,** 10687 (2017).

[25] I. Freund, Looking through Walls and around Corners, Physica A **168,** 49 (1990).

[26] O. Katz, P. Heidmann, M. Fink, and S. Gigan, Non-invasive single-shot imaging through scattering layers and around corners via speckle correlations, Nat. Photonics **8,** 784 (2014).

[27] K. Lee and Y. Park, Exploiting the speckle-correlation scattering matrix for a compact reference-free holographic image sensor, Nat. Commun. **7,** 13359 (2016).

[28] H. Yu, T. R. Hillman, W. Choi, J. O. Lee, M. S. Feld, R. R. Dasari, and Y. Park, Measuring Large Optical Transmission Matrices of Disordered Media, Phys.l Rev. Appl. **111,** 153902 (2013).

[29] I. Reed, On a moment theorem for complex Gaussian processes, IRE Trans. Inf. Theory **3,** 194 (1962).

[30] A. V. Balakrishnan, *Introduction to Random Processes in Engineering* (Wiley, New York, NY, USA, 1995).

[31] P. A. Lemieux and D. J. Durian, Investigating non-Gaussian scattering processes by using nth-order intensity correlation functions, J. Opt. Soc. Am. A **16,** 1651 (1999).

[32] L. Isserlis, On a formula for the product-moment coefficient of any order of a normal frequency distribution in any number of variables, Biometrika **12,** 134 (1918).

[33] D. B. Conkey, A. M. Caravaca-Aguirre, and R. Piestun, High-speed scattering medium characterization with application to focusing light through turbid media, Opt. Express **20,** 1733 (2012).

[34] G. Lai and T. Yatagai, Generalized Phase-Shifting Interferometry, J. Opt. Soc. Am. A **8,** 822 (1991).

[35] J. Yoon, K. Lee, J. Park, and Y. Park, Measuring optical transmission matrices by wavefront shaping, Opt. Express **23,** 10158 (2015).

[36] S. Shin, K. Lee, Y. Baek, and Y. Park, Reference-Free Single-Point Holographic Imaging and Realization of an Optical Bidirectional Transducer, Phys. Rev. Appl. **9,** 044042 (2018).

[37] A. Boniface, M. Mounaix, B. Blochet, R. Piestun, and S. Gigan, Transmission-matrix-based point-spread-function engineering through a complex medium, Optica **4,** 54 (2017).

[38] A. Dremeau, A. Liutkus, D. Martina, O. Katz, C. Schulke, F. Krzakala, S. Gigan, and L. Daudet, Reference-less measurement of the transmission matrix of a highly scattering material using a DMD and phase retrieval techniques, Opt. Express **23,** 11898 (2015).

[39] S. A. Alexandrov, T. R. Hillman, T. Gutzler, and D. D. Sampson, Synthetic Aperture Fourier Holographic Optical Microscopy, Phys. Rev. Lett. **97,** 168102 (2006).

[40] V. Mico, Z. Zalevsky, P. Garcia-Martinez, and J. Garcia, Superresolved imaging in digital holography by superposition of tilted wavefronts, Appl. Opt. **45,** 822 (2006).

[41] V. Mico, Z. Zalevsky, P. Garcia-Martinez, and J. Garcia, Synthetic aperture superresolution with multiple off-axis holograms, J. Opt. Soc. Am. A **23,** 3162 (2006).

[42] M. Takeda, H. Ina, and S. Kobayashi, Fourier-transform method of fringe-pattern analysis for computer-based topography and interferometry, J. Opt. Soc. Am. **72,** 156 (1982).

[43] E. Cuche, P. Marquet, and C. Depeursinge, Simultaneous amplitude-contrast and quantitative phase-contrast microscopy by numerical reconstruction of Fresnel off-axis holograms, Appl. Opt. **38,** 6994 (1999).

[44] I. I. Freund, M. Rosenbluh, and S. Feng, Memory Effects in Propagation of Optical Waves Through Disordered Media, Phys. Rev. Lett. **61,** 2328 (1988).

[45] B. Judkewitz, R. Horstmeyer, I. M. Vellekoop, I. N. Papadopoulos, and C. H. Yang, Translation correlations in anisotropically scattering media, Nat. Phys. **11,** 684 (2015).

[46] G. Osnabrugge, R. Horstmeyer, I. N. Papadopoulos, B. Judkewitz, and I. M. Vellekoop, Generalized optical memory effect, Optica **4,** 886 (2017).

[47] J. Bertolotti, E. G. van Putten, C. Blum, A. Lagendijk, W. L. Vos, and A. P. Mosk, Non-invasive imaging through opaque scattering layers, Nature **491,** 232 (2012).

[48] A. K. Singh, D. N. Naik, G. Pedrini, M. Takeda, and W. Osten, Exploiting scattering media for exploring 3D objects, Light-Sci. Appl. **6**, e16219 (2017).

[49] H. He, Y. Guan, and J. Zhou, Image restoration through thin turbid layers by correlation with a known object, Opt. Express **21**, 12539 (2013).

[50] Y. Choi, M. Kim, C. Yoon, T. D. Yang, K. J. Lee, and W. Choi, Synthetic aperture microscopy for high resolution imaging through a turbid medium, Opt. Lett. **36**, 4263 (2011).

[51] J. Goodman, W. Huntley Jr, D. Jackson, and M. Lehmann, Wavefront-reconstruction imaging through random media, Appl. Phys. Lett. **8**, 311 (1966).

[52] E. N. Leith and J. Upatnieks, Holographic imagery through diffusing media, J. Opt. Soc. Am. A **56**, 523 (1966).

[53] H. Kogelnik and K. Pennington, Holographic imaging through a random medium, J. Opt. Soc. Am. A **58**, 273 (1968).

[54] W. Harm, C. Roider, A. Jesacher, S. Bernet, and M. Ritsch-Marte, Lensless imaging through thin diffusive media, Opt. Express **22**, 22146 (2014).

[55] A. K. Singh, D. N. Naik, G. Pedrini, M. Takeda, and W. Osten, Looking through a diffuser and around an opaque surface: A holographic approach, Opt. Express **22**, 7694 (2014).

[56] M. J. Purcell, M. Kumar, S. C. Rand, and V. Lakshminarayanan, Holographic imaging through a scattering medium by diffuser-aided statistical averaging, J. Opt. Soc. Am. A **33**, 1291 (2016).

[57] R. K. Singh, A. M. Sharma, and B. Das, Quantitative phase-contrast imaging through a scattering media, Opt. Lett. **39**, 5054 (2014).

[58] A. S. Somkuwar, B. Das, R. V. Vinu, Y. Park, and R. K. Singh, Holographic imaging through a scattering layer using speckle interferometry, J. Opt. Soc. Am. A **34**, 1392 (2017).

[59] B. Das, N. S. Bisht, R. V. Vinu, and R. K. Singh, Lensless complex amplitude image retrieval through a visually opaque scattering medium, Appl. Opt. **56**, 4591 (2017).

[60] J. Park, J. Y. Cho, C. Park, K. Lee, H. Lee, Y. H. Cho, and Y. Park, Scattering optical elements: Stand-alone optical elements exploiting multiple light scattering, ACS Nano **10**, 6871 (2016).

[61] M. K. Kim, Principles and techniques of digital holographic microscopy, SPIE Rev. **1**, 018005 (2010).

[62] G. Popescu, Quantitative phase imaging of nanoscale cell structure and dynamics, Methods Cell Biol. **90**, 87 (2008).

[63] P. Memmolo, L. Miccio, M. Paturzo, G. Di Caprio, G. Coppola, P. A. Netti, and P. Ferraro, Recent advances in holographic 3D particle tracking, Adv. Opt. Photonics **7**, 713 (2015).

[64] K. Lee, K. Kim, J. Jung, J. Heo, S. Cho, S. Lee, G. Chang, Y. Jo, H. Park, Y. Park, Quantitative phase imaging techniques for the study of cell pathophysiology: From principles to applications, Sensors **13**, 4170 (2013).

[65] K. Kim, J. Yoon, S. Shin, S. Lee, S.-A. Yang, and Y. Park, Optical diffraction tomography techniques for the study of cell pathophysiology, J. Biomed. Photonics Eng. **2**, 020201 (2016).

[66] G. Young *et al.*, Quantitative mass imaging of single biological macromolecules, Science **360**, 423 (2018).

[67] C. W. Hsu, S. F. Liew, A. Goetschy, H. Cao, and A. D. Stone, Correlation-enhanced control of wave focusing in disordered media, Nat. Phys. **13**, 497 (2017).

[68] S. A. Prahl, M. J. van Gemert, and A. J. Welch, Determining the optical properties of turbid media by using the adding–doubling method, Appl. Opt. **32**, 559 (1993).

[69] W. H. Lee, Binary synthetic holograms, Appl. Opt. **13**, 1677 (1974).